### Title
Nonspherical laser-induced cavitation bubbles




### Journal
Physical Review E, 81(1)

### ISSN
2470-0045



### Authors
Lim, Kang Yuan
Quinto-Su, Pedro A
Klaseboer, Evert
et al.



### Publication Date
2010

### DOI
10.1103/physreve.81.016308

# Nonspherical laser-induced cavitation bubbles

Kang Yuan Lim,[1] Pedro A. Quinto-Su,[1] Evert Klaseboer,[2] Boo Cheong Khoo,[3] Vasan Venugopalan,[4] and Claus-Dieter Ohl[1]
[1]*Division of Physics and Applied Physics, School of Physical and Mathematical Sciences, Nanyang Technological University, 21 Nanyang Link, Singapore 637371, Singapore*
[2]*Institute of High Performance Computing, Fusionopolis, 1 Fusionopolis Way, #16-16 Connexis, Singapore 138632, Singapore*
[3]*Department of Mechanical Engineering, National University of Singapore, 10 Kent Ridge Crescent, Singapore 119260, Singapore*
[4]*Department of Chemical Engineering and Materials Science and Laser Microbeam and Medical Program, Beckman Laser Institute, University of California, Irvine, California 92697-2575, USA*
(Received 11 October 2009; published 14 January 2010)

The generation of arbitrarily shaped nonspherical laser-induced cavitation bubbles is demonstrated with a optical technique. The nonspherical bubbles are formed using laser intensity patterns shaped by a spatial light modulator using linear absorption inside a liquid gap with a thickness of 40 $\mu$m. In particular we demonstrate the dynamics of elliptic, toroidal, square, and V-shaped bubbles. The bubble dynamics is recorded with a high-speed camera at framing rates of up to 300 000 frames per second. The observed bubble evolution is compared to predictions from an axisymmetric boundary element simulation which provides good qualitative agreement. Interesting dynamic features that are observed in both the experiment and simulation include the inversion of the major and minor axis for elliptical bubbles, the rotation of the shape for square bubbles, and the formation of a unidirectional jet for V-shaped bubbles. Further we demonstrate that specific bubble shapes can either be formed directly through the intensity distribution of a single laser focus, or indirectly using secondary bubbles that either confine the central bubble or coalesce with the main bubble. The former approach provides the ability to generate in principle any complex bubble geometry.

DOI: 10.1103/PhysRevE.81.016308 PACS number(s): 47.55.dp, 47.55.dd, 47.61.Jd

## I. INTRODUCTION

Short-lived vapor bubbles created by focusing pulsed-laser light have demonstrated exciting properties for the actuation of fast flows in microfluidics and the manipulation of small objects. These laser-induced cavitation bubbles can be utilized for the lysis of cells [1–4], the creation of pores in cell membranes [5], for microfluidic operations such as switching [6], pumping, and mixing [7,8]. Due to the very fast bubble dynamics, fluid actuation on the microsecond time scale and the creation of very high levels of normal and shear stresses can be achieved. In contrast conventional microfluidic operating conditions are typically in the low Reynolds number regime.

Two physical mechanisms for bubble creation with lasers can be identified: heating and vaporization of the fluid with and without stress confinement [9] due to linear absorption and optical breakdown [10–12]. In the case of stress confinement, the laser energy is absorbed in the liquid and the cavitation bubble results from an explosive vaporization. In optical breakdown, a plasma is formed at the focal volume of the focused laser pulse and drives the early stage of bubble expansion. Generally, the initial shape of the cavitation bubble and its induced flow field is determined by the spatial distribution of the injected energy, i.e., the focal volume of the laser irradiation. Only at later times do the boundaries of the fluid domain affect the bubble dynamics.

The generic example of a boundary induced bubble shape is the single laser-induced bubble at a variable distance from a rigid boundary [13]. Depending on the distance of the bubble to the boundary the bubble may obtain a spherical, an approximate oblate spheroidal, or a hemispherical shape at maximum expansion. During shrinkage, the so-called collapse, the bubble develops a jetting flow toward the boundary. Nonspherical, elongated bubbles have also been observed as an effect of weak focusing, in particular for subnanosecond lasers pulses using low numerical aperture focusing lenses, leading to a filamentous optical breakdown structure [10,14]. In contrast, here we deliberately modify and control the shape of the focused laser pulse such as to induce a nonspherical bubble shape from the beginning of the bubble dynamics. These shaped bubbles then lead to a nonradial flow with novel properties which may be exploited. For example microrheology depends on the specific forcing of the object under test. This may be achieved through purely extensional or compressional flows. Although we do not study the properties of each of the new bubble shapes, the toroidal bubble is a prospective candidate to generate a purely compressional flow.

We demonstrate here how to extend the current techniques and to create nonradial flows. Our long-term goal is to create on-demand flow patterns from well controlled bubble shapes and arrangements for pulsed-laser only controlled microfluidic actuation.

We have demonstrated that complex bubble patterns can be generated using a holographic element [15]. For these devices the intensity distribution is related to the pattern displayed on the spatial light modulator (SLM)—acting as a phase object—by a Fourier transform. In previous works multiple circular foci were generated to create arbitrary arrangements of spherical bubbles. Here, we report on deliberately changing the intensity distribution to create nonspherical bubbles and study their dynamics using high-speed photography. Additionally, we compare the bubble dynamics with the solution from an axisymmetric potential flow solver [16,17].

 

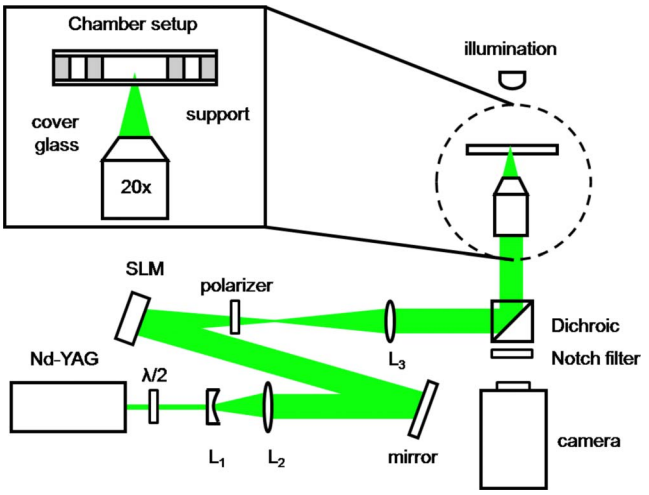


FIG. 1. (Color online) Experimental setup. Cavitation bubbles are generated with a pulsed laser reflected from a digital spatial light modulator (SLM) which is focused after passing through several optics into a thin liquid film with a 20× microscope objective. The liquid film is contained in a chamber of 40 $\mu$m height which is filled with a light absorbing aqueous yellow ink. The fast bubble dynamics is studied with a high-speed camera.

This work is organized as follows: we begin with a presentation of the experimental setup to create and observe the bubbles and a brief description of the numerical method. Then, we present a series of nonspherical bubbles, e.g., elliptic, toroidal, and V-shaped bubbles, created by shaping the focused intensity distribution of the laser into a line, circle, and v-shape, respectively. Next, we demonstrate that nonspherical, e.g., square bubbles, can also be generated through "secondary bubbles" (patterns with multiple foci) with and without bubble coalescence. We discuss several aspects of the observed dynamics such as eccentricity, jetting, and potential applications.

## II. EXPERIMENTAL SETUP

In our experimental setup the bubbles are created through linear absorption of pulsed-laser light which leads to a superheated region which eventually explodes into a vaporous cavity [18]. The laser beam is focused through a microscope objective (20×, NA 0.7) at the bottom of a chamber filled with the absorbing liquid.

To create nonspherical bubbles the light intensity distribution at the focal plane is shaped with a spatial light modulator (SLM, model LC-R-2500, Holoeye Photonics, Germany). The SLM is a two-dimensional reflective array where each pixel acts as a variable phase plate which can be individually addressed by a computer. Illuminating the SLM with a collimated beam and focusing the reflected light with a lens leads to an intensity distribution at the lens' focal plane which is related to the SLM pattern through a Fourier transform [15,19].

Figure 1 shows a schematic of the experimental setup: a frequency doubled Nd:YAG laser (New Wave, Fremont, CA) emits pulses with a temporal width of 6 ns at a wavelength of $\lambda=532$ nm. The polarization of the laser pulse is rotated with a half wave plate (indicated a $\lambda/2$ in Fig. 1). A telescope formed by the lenses $L_1$ and $L_2$ expands the beam to cover the surface of the SLM. In order to remove the zero-order undiffracted part of the beam [15], a lens phase is added to the hologram displayed at the SLM. Additionally a third lens $L_3$ images the SLM onto the back aperture of the microscope objective (20×, NA 0.7) mounted on an inverted microscope (Olympus IX-71). The pattern is projected at the bottom of the liquid gap. The imaging is done using the same objective that is used to deliver the beam into the sample [15]. The sample is illuminated with the microscope condenser and the dynamics of the bubbles are recorded with a high-speed camera (Photron SA1, San Diego, CA) at frame rates of up to 300 000 frames per second.

The liquid film is confined by two No. 1 microscope coverslips separated with spacers (made of aluminum foil, inset Fig. 1). The size of the chamber is $20\times20$ mm$^2$ laterally and has a height of 40 $\mu$m. We are using yellow inkjet printer ink (Maxtec Inc., Hongkong) that absorbs the green light from the laser and is sufficiently transparent for the illumination light from the microscope condenser to obtain high framing speeds. The aqueous ink has a density $\rho=1046$ kg/m$^3$ and a dynamic viscosity of $\mu=2.14\times10^{-3}$ Pa s at room temperature.

## III. SIMULATIONS

To obtain more insight into the fluid flow we compare the experimental high-speed recordings with simulations using a boundary element method (BEM) for potential flow basically similar to those used in [16,17,20]. More information on the use of boundary element methods for bubble dynamics can be found in [21–23]. In using this model, we neglect viscous effects in the fluid, at the rigid boundaries and the bubble interface. It can be argued that viscous effects from boundary layers may not be important for sufficiently short times; their growth is governed by a diffusive time scale, $\tau\approx y^2/\nu$, where $y$ is a characteristic length and the $\nu$ is the kinematic viscosity. If we identify $y$ with half the channel height, i.e., 20 $\mu$m and the kinematic viscosity $\nu=\mu/\rho\approx2\times10^{-6}$ m$^2$ s$^{-1}$ the diffusive time of boundary layer growth is of the order of 0.2 ms, about ten times longer than the oscillation period of the bubble.

For potential flow, if the velocity vector, $\mathbf{u}$, anywhere in the flow and the potential $\Phi$ are related as $\mathbf{u}=\nabla\Phi$ and furthermore the Laplace equation holds: $\nabla^2\Phi=0$ in the fluid domain. The boundary element method makes use of the fact that if the potential (Dirichlet condition) is given on the bubble surface $S$, the solution of the Laplace equation is unique. That is, the normal derivative of the potential, $\partial\Phi/\partial n$, (Neumann condition with $\partial/\partial n=\mathbf{n}\cdot\nabla$ the normal inward derivative at the boundary) is unique. The vector $\mathbf{n}$ is the normal vector on $S$ and is directed out of the fluid. $S$ is assumed to be the only surface for this particular problem. The quantity $\partial\Phi/\partial n$ is also equal to the normal velocity at the surface. The BEM method exploits this by using a boundary integral formulation as

$$c(\mathbf{x})\Phi(\mathbf{x}) + \int_S \Phi(\mathbf{y})\frac{\partial G(\mathbf{y},\mathbf{x})}{\partial n}dS = \int_S G(\mathbf{y},\mathbf{x})\frac{\partial \Phi(\mathbf{y})}{\partial n}dS. \tag{1}$$

in which $\boldsymbol{x}$ is a fixed point and $\boldsymbol{y}$ the integration variable both located on $S$ and $c(\mathbf{x})$ is the solid angle at location $\boldsymbol{x}$. $G$ is the Green function or kernel function defined in a three-dimensional (or axial symmetric) domain as $G(\mathbf{y},\mathbf{x}) = 1/|\mathbf{x}-\mathbf{y}|$. Equation (1) provides a means to calculate the normal velocity at the bubble surface if the potential is known. This is done by dividing the bubble surface in (initially equally spaced) nodes connected by elements and transforming Eq. (1) into a matrix—vector equation, which can be solved for the unknown velocities. The pressure of the bubble for a time-dependant problem applicable at the bubble interface equals (using the Bernoulli equation),

$$p = p_{\text{ref}} - \rho\frac{D\Phi}{Dt} + \frac{1}{2}\rho|\mathbf{u}|^2. \tag{2}$$

Here $\rho$ is the density of the liquid surrounding the bubble, $t$ represents time, and $p_{\text{ref}}$ the reference pressure (taken to be atmospheric pressure here). The material derivative $D/Dt = \partial/\partial t + \mathbf{u}\bullet\nabla$ is used, since the potential on the moving bubble surface is needed for the BEM. An adiabatic uniform pressure is assumed inside the bubble as $p = P_0(V_0/V)^\gamma$, where $P_0$ and $V_0$ are the initial pressure and volume of the bubble. It is important to note that we model the bubble interior as an ideal thus noncondensable gas with a constant ratio of the specific heats of $\gamma = 1.25$. This value is only an educated guess as we basically ignore the complex thermodynamic processes of the gas and vapor mixture inside the bubble. The value of $\gamma = 1.25$ has been chosen to account for the heat losses during the late expansion and early collapse dynamics and the adiabatic bubble wall during the faster dynamics. This approximation follows also Cole's model for an underwater explosion [24].

The BEM method now works as follows:

(1) Assume a bubble with the desired initial shape (square, elliptic, etc.) with initial volume $V_0$ and pressure $P_0$.

(2) Calculate the potential at the next time step using a time discretized version of Eq. (2).

(3) Then use Eq. (1) to get the corresponding normal velocities with which the bubble surface is updated.

(4) Calculate the new volume, pressure and velocity at each node.

(5) Go to the next time step and repeat steps (2) to (4) as many times as required.

The interested reader is referred to Refs. [16,17] for the details on the numerical implementation.

Besides the neglect of viscous effects, a second simplification of our model is the axisymmetry formulation, i.e., we compare the experimental pictures with an appropriate plane cut through the simulated axisymmetric volume. As demonstrated in Fig. 2 we compare all nonspherical geometries to the plane $\varphi = \text{const}$ of the axisymmetric volume $(r,z,\varphi)$ except for the toroidal bubble where both the plane $z=0$ and $\varphi = \text{const}$ are investigated.

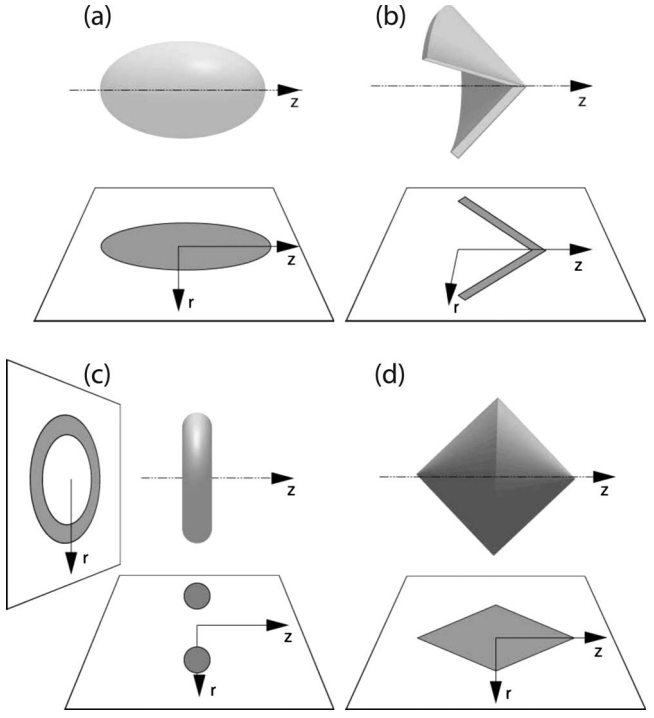


FIG. 2. Geometry of the axisymmetric bubble simulations and the resulting planes used to compare with the high-speed photography. The axis of symmetry is the $z$ axis. For the elliptic (a), the v-shaped (b), and the square bubble (d) we compare the bubble dynamics to the projection in the $rz$ plane of an ellipsoidal, hollow cone, and double cone, respectively. The toroidal bubble (c) in the experiments is compared to its projection in the $r\varphi$ plane and the $rz$ plane.

The influence of the confining lower and upper plates placed at a distance of 40 $\mu$m is not accounted for in the axisymmetric formulation. Only a fully three-dimensional simulation would take care of the experimental geometry.

Consider a point like laser focus, which would create a single laser bubble in an infinite medium. Here, because the laser is focused just above the lower boundary, see inset of Fig. 1, a mostly hemispherical bubble will emerge. We expect that the second boundary is mostly slowing down the bubble dynamics through the confinement of the liquid. For example, when the bubble shrinks, less liquid is available to accelerate the bubble interface and the bubble shrinks slower as compared to an infinite liquid. The boundaries will also affect the bubble shape during the last stage of the bubble. Here, we expect that for close distances between the plates jetting toward the upper boundary will be induced.

The initial conditions for the simulations are chosen by adjusting the initial pressure inside the bubble and its initial volume. Further simplifications of the model are the neglect of surface tension and gravity as they have only minor effects on the bubble dynamics for the bubble sizes in the experiments. The simulations start with an initial pressure of $P_0(t=0) = 50$ bar.

The simulations are performed in such a way to get a matching experimental and numerical maximum bubble radius, $R_{\text{max}}$. To compare the simulations with the experiments we have to deal with the retardation effect induced by the

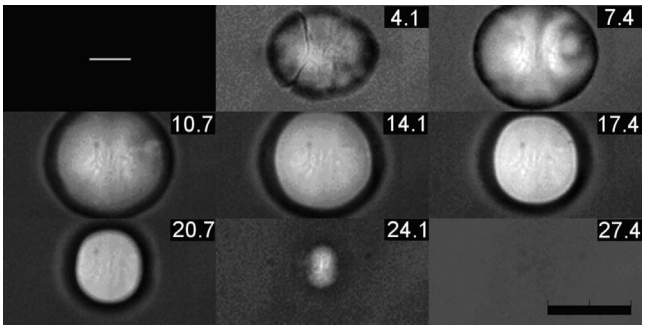


FIG. 3. Experimental observation of an elliptical bubble with eccentricity inversion. The bubble is generated with a longer horizontal shape but during the collapse phase the vertical dimension becomes larger. First frame represents the image used to shape the laser focus (frame rate 300 000 fps, exposure time 1.76 $\mu$s, laser energy 22 $\mu$J). The top right corner shows the time after the laser pulse in microseconds and the black bar denotes 100 $\mu$m and the time stamps in the upper right are given in microseconds.

narrow gap. Interestingly, the ratio between the experimental bubble lifetime, $T_{exp}$, and the simulated dimensional time, $T_{sim}$, is $T_{exp}/T_{sim} \approx 1.7$ for all bubbles. The time in the experiments and the simulations was normalized with the bubble lifetime. In this way the normalized dimensionless time, $t'$, lies in the interval [0,1] and we plot the simulated frames that correspond to the experimental ones on the normalized time scale.

## IV. NONSPHERICAL BUBBLE GENERATION BY SHAPING THE LASER INTENSITY DISTRIBUTION

In all figures showing the bubble dynamics we will depict in the first frame the intensity profile in black and white which is used to calculate the hologram. This frame reflects the ideal intensity distribution of the laser radiation in the focal plane.

### A. Elliptic bubble

Figure 3 shows the dynamics of a bubble created from focusing the light on a line leading to an essentially elliptical bubble. The high-speed sequence is recorded at 300000 fps. On the second frame, $t=4.1$ $\mu$s, the bubble is fragmented, yet it coalesces quickly into one bubble at 7.4 $\mu$s. The horizontal extent of the bubble, $a$, is still larger than the vertical one, $b$, such that the eccentricity, $\varepsilon=a/b$, is still larger than 1. On the next frame (10.7 $\mu$s) the bubble has taken on an almost spherical shape, with an eccentricity very close to 1.0. At times 20.7 $\mu$s and at 24.1 $\mu$s (just before collapse) we can see clearly that the vertical dimension is now larger than the horizontal one, so that the eccentricity is smaller than 1. The phenomenon of inversion of the eccentricity was typical for all elliptic bubbles in this study.

Figure 4 shows the result of the simulations for the evolution of an elliptical bubble that expands against the hydrostatic pressure. The snapshots of the bubble are taken at the same relative instants as shown in the experiment, Fig. 3

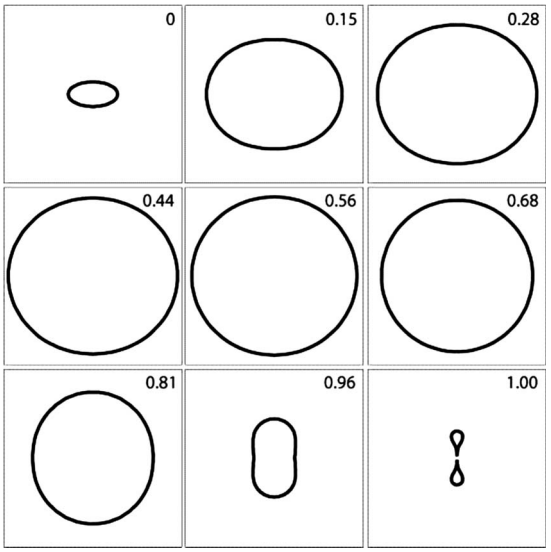


FIG. 4. Numerical simulation of an elliptic bubble, with an initial pressure of $P_0(t=0)=50$ bar. When compared to Fig. 3 similar phenomena can be observed: an initially elliptic bubble with longer horizontal axis turns into an almost spherical bubble during its maximum size and then collapses with a longer vertical axis. The breakup of the bubble as shown in the last frame could not be observed in the experiment, likely due to a lack of temporal resolution.

using $T_{exp}/T_{sim}=1.76$ and an experimental lifetime of $T_{exp}=25$ $\mu$s. We observe the same trend as in the experiment, the major axis, $a$, of the initial elliptical bubbles collapses faster than the minor axis, $b$. Thus, the eccentricity reverses during the collapse of the bubble. The simulations also show a ring-jet formed during the collapse created along the initial major axis. Even though the curvature in the last frame of Fig. 4 is relatively high, the physics is still dominated by inertial effects due to the high velocities occurring at this instant. Surface tension effects are thus still small. In the experiments we did not observe the jets, likely because the recording was not fast enough, the jets would appear between the times $t=24.1$ $\mu$s and $t=27.4$ $\mu$s in Fig. 3. Note that the relative timing from the last two images is 0.96 to 1.00, thus the collapse takes place very fast (only 4% of the lifetime of the bubble). Although some blurring on the left and right of the experimental bubble at $t=24.1$ $\mu$s may hint to a developing jet. To strengthen the statement of eccentricity inversion we present a quantitative comparison of the eccentricities as a function of time in Fig. 5. Experiment and simulations agree within the experimental uncertainty.

### B. V-shaped bubble

More complex bubble dynamics results from two linear focusing regions connected under some angle, i.e., forming a V-shaped focus. This shape is shown in the first frame of Fig. 6. The bubble expands and up to $t=12.6$ $\mu$s with some cleavages visible. The bubble reaches its maximum size at $t=15.3$ $\mu$s. At $t=17.9$ $\mu$s, the bubble shape starts to transform into a triangular shape pointing in a direction opposite to the initial orientation of the bubble. This shape remains

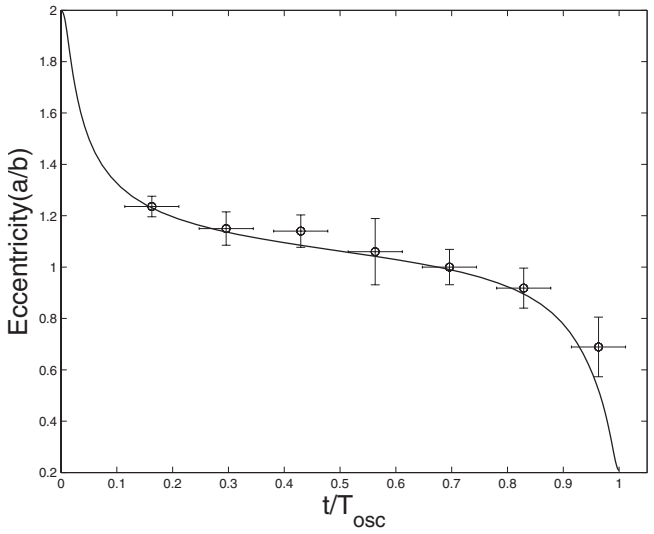


FIG. 5. This graph shows the eccentricity $(a/b)$, where $a$ is the horizontal axis and $b$ the vertical axis of the bubble. The squares correspond to the experiment shown in Fig. 3 and the solid line is the BEM simulations.

until the bubble collapse. The corresponding simulation is shown in Fig. 7, where $T_{exp}/T_{sim}=1.70$ and an experimental lifetime of $T_{exp}=36$ $\mu$s. The bubble shape evolves in a very similar way as the experimental one, e.g., at time $t'=0.86$ a similar reversed triangular shape is found. Interestingly, numerically the collapse scenario is rather complex with the formation of multiple jets, one from the right pointed tip, and two counterpropagating jets from below and above.

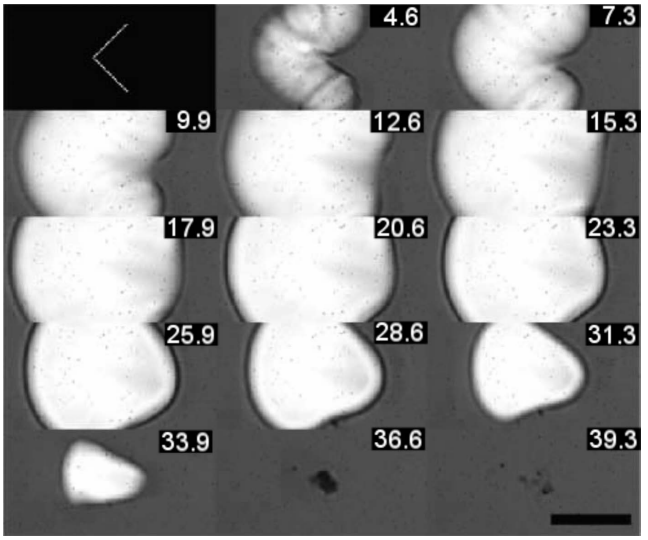


FIG. 6. Experimental observation of a more complex bubble dynamics emerging from a V-shaped focus. The recording shows selected frames taken at 300 000 fps with an exposure time of 2.2 $\mu$s, laser energy of 58 $\mu$J. The dots in the frames are from 3 $\mu$m diameter polystyrene particles used for flow visualization. The black bar denotes a length of 100 $\mu$m and the time stamps in the upper right are given in microseconds.

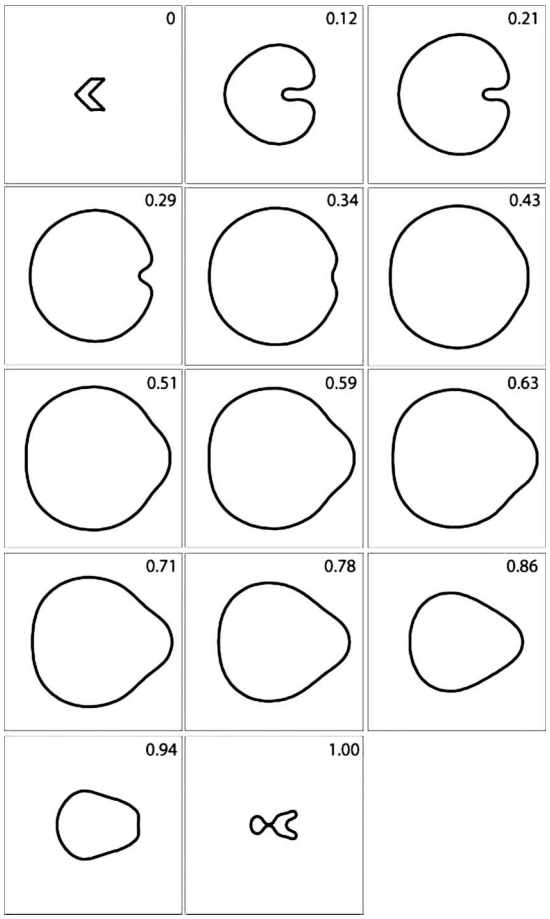


FIG. 7. Simulation of a V-shaped bubble: the initially V-shaped bubble quickly turns into a more rounded shape. The "hollow" part of the V shape remains visible for quite some time, but finally disappears at $t'\sim 0.4$. It then overshoots and becomes a bulge clearly visible at the right-hand side of the bubble. This bulge develops into a jet from $t'=0.94$ onward. A ring jet is formed in the left central section of the bubble. Once this jet impacts the simulations are being stopped. The jet from the right hand side has not yet fully penetrated the bubble at this instant. The axis of symmetry is the $z$ axis.

### C. Toroidal bubble

Figure 8 demonstrates the dynamics of a toroidal bubble created by shaping the beam into the circle shown on the first frame. At time $t=3.7$ $\mu$s after the laser pulse arrival we see a nonsmooth bubble surface, indicating that the torus consists of distinct and rapidly expanding bubbles. The fragmented structure already smoothened at 7.7 $\mu$s, likely because of coalescence and some out of focus movement of parts of the bubble interface. The toroidal bubble continues to expand until it reaches its maximum size at 35.7 $\mu$s, and then starts collapsing. The darker region in the center is probably due to a remaining liquid core in the center of the torus, thus the torus retains its shape during the expansion-collapse cycle.

The simulations in Fig. 9 show both the top view, Fig. 9(a), and the cross section of the torus, Fig. 9(b). Interestingly, a toroidal bubble develops an annular jet toward its

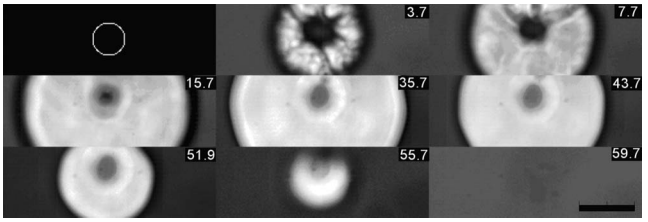


FIG. 8. Toroidal bubble created from a circular focus depicted in the first frame. The bubble expands initially with a rough surface likely due to separate bubbles which only coalesce in a later stage. Please note that the bubble retains its toroidal shape during the expansion and collapse cycle. The recording is taken at a frame rate of 250 000 fps with an exposure time of 1.8 $\mu$s and laser energy of 51.8 $\mu$J. The black bar denotes a length of 100 $\mu$m and the time stamps in the upper right are given in microseconds.

center. This behavior can be understood with the center-of-mass moving toward the torus center during the shrinkage. According to Benjamin and Ellis [25] any moving and shrinking bubble develops a jet in the direction of motion. Such a jet could not be observed in the experiments (since it happens out of the viewing point of the camera), but is very

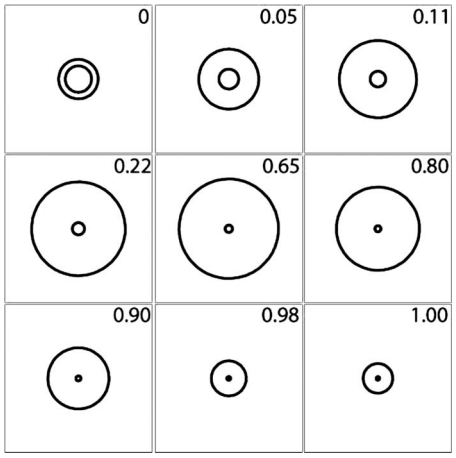


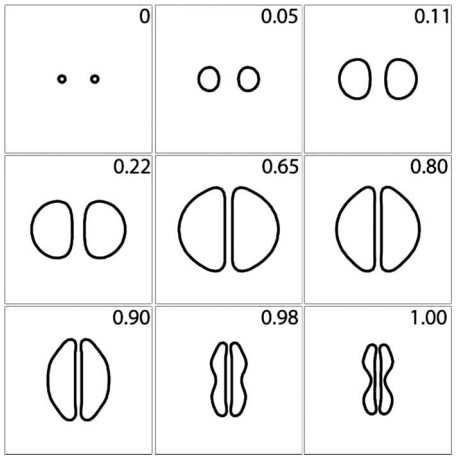


FIG. 9. Two cross sections of the toroidal bubble simulation results for (a) the $r\varphi$ plane (to be compared with Fig. 8), (b) the $rz$ plane.

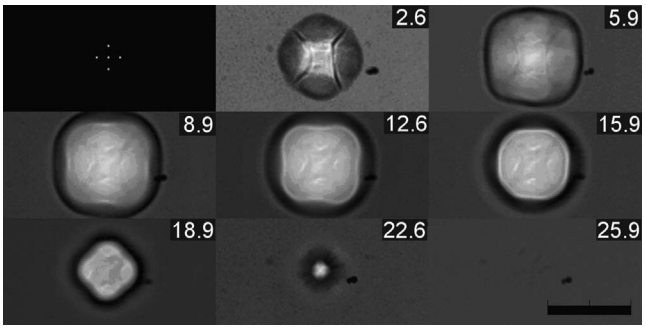


FIG. 10. Coalescence method to create a square bubble. The laser is focused onto five distinct but near by spots as depicted in the first frame. All five bubbles quickly expand and are already merged into one bubble at $t=5.9$ $\mu$s. Please note the diamond shape of the bubble during collapse. The frames are selected from a recording taken at 300 000 fps with an exposure time of 1.8 $\mu$s. The laser energy to all five spots is 20 $\mu$J. The black bar denotes a length of 100 $\mu$m and the time stamps in the upper right are given in microseconds.

likely to be present. This example shows the advantages of the numerical simulations: it can show details that otherwise would not have been observable. In this simulation $T_{exp}/T_{sim}=1.64$ and the experimental lifetime is $T_{exp}=56$ $\mu$s.

## V. SQUARE BUBBLE GENERATION WITH MULTIPLE LASER FOCI

Multiple distinct bubbles can be created using multiple laser foci. We have observed that these bubbles may coalesce depending on the laser energy attributed to each focus and their distance. This gives the possibility to create nonspherical bubbles through bubble-bubble coalescence. Yet, we also were able to constrain the shape of a central bubble by surrounding it with "helper" bubbles and without coalescence to occur.

### A. Method using bubble coalescence

Here, five bubbles are nucleated and quickly coalesce into one large square bubble, visible at $t=5.9$ $\mu$s in Fig. 10. The square shape is stable during bubble expansion. During the collapse however, the bubble rounds up visibly at time $t=15.9$ $\mu$s and then it develops a diamond shape at $t=18.9$ $\mu$s. Shortly afterward jets emerge from all four corners in which the fast motion resulted in a blurred image at time $t=22.6$ $\mu$s in Fig. 10. Some structure inside the bubble is evident which we attribute to the remains of the liquid films from the coalescence process.

The simulation of this geometry, Fig. 11, is started with a diamond shaped bubble resembling the configuration of bubbles shortly after the generation, with $T_{exp}/T_{sim}=1.68$ and the experimental lifetime of $T_{exp}=23$ $\mu$s. Thus we ignore the time before coalescence. The bubble expands to a square shape quickly and collapses with the rotation of its shape by 45°, resulting again into a diamond shape. The last frame in the simulation does not compare with the experiment and is depicting the already re-expanding bubbles. Likely this is

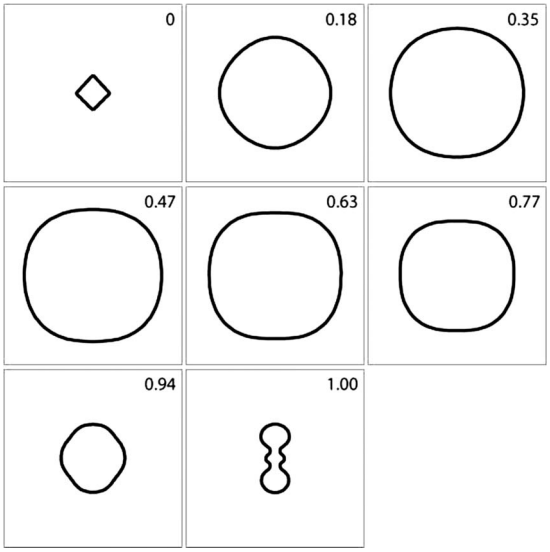


FIG. 11. Simulation of the square bubble dynamics without the bubble-bubble coalescence. The bubble starts with a diamond shape resembling the shape of the focus, see first frame of Fig. 10. The last frame shows distinct differences compared to the experiment which we contribute to residual gas pressure.

due to the higher gas pressure in the simulated bubbles, thereby allowing for lesser compression. Therefore, the bubble re-expands before it develops the four jets which are weakly visible in the experiment, Fig. 10.

### B. Method without bubble coalescence

In Fig. 12 four bubbles are used to confine a central bubble into a rotated square shape. The laser energy is approximately the same as in Fig. 10, yet the distance between the foci is increased by almost a factor of two. Therefore, the films between the bubbles do not drain and we see the expansion and collapse of the five individual bubbles. The interfaces between the outer "helper" bubbles and the central bubble flatten during expansion which leads to a transformation of the initially curved interfaces at $t=4.1$ $\mu$s to flat interfaces at $t=10.7$ $\mu$s. The flattening of the liquid film between two close bubbles has been observed before [26,27]. Also the center bubble is shielded by the surrounding bubbles leading to a low pressure region. The center bubble only collapses after the shielding has ended; it therefore shows a delayed collapse [26]. Interestingly the four "helper" bubbles jet toward the central bubble during their collapse which is visible at $t=14.1$ $\mu$s and $t=17.4$ $\mu$s.

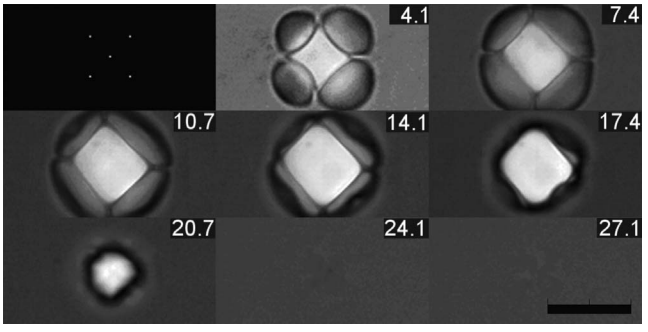


FIG. 12. Creation of a rotated square bubble by confining the expansion of a central bubble with four helper bubbles. The larger distance between the laser foci (first frame) suppressed the coalescence although as similar laser energy of 26 $\mu$J is used. Selected frames taken at 300 000 fps with an exposure time of 1.8 $\mu$s. The black bar denotes a length of 100 $\mu$m.

## VI. DISCUSSIONS

Nonspherical bubbles, in particular elliptic, V-shaped, and toroidal bubbles can be created with a single focus on a line, see Figs. 3, 6, and 8. A closer look of the initial bubble shape created reveals that the resulting surface is not smooth but shows crack like structures which we attribute to the interface between explosively expanding bubbles. Only the coalescence of these initial bubbles leads to later desired smooth shapes.

For the coalescence to occur the separating films have to be thinned and drained by the expanding bubbles. Although the surface of the bubble afterward is smooth, some structures remains visible, e.g., in Fig. 3 at 7.4 $\mu$s. We speculate that these features may be remnants from the liquid films separating the bubbles and rupturing just before the coalescence. Similar structures are seen for all other experiments except the noncoalescing bubbles shown in Fig. 12. This observation suggests that all of the nonspherical bubbles except for Fig. 12 are formed through coalescence of smaller bubbles during their explosive growth. Unfortunately, the temporal resolution of our experiment does not allow the study of this coalescence process for Figs. 3, 6, and 8.

The bubbles are created through linear absorption. After the laser pulse, pressure and tension waves emerge and superimpose over the illuminated region leading to a complex acoustic diffraction pattern [28]. Likely these thermoelastic waves [29] lead to some instability and growth of distinct bubbles. Bubble nucleation from a line focus may therefore be inherently unstable due to these acoustic interactions. However, for certain configurations as shown in this work at some later times coalescence is obtained and a single bubble of the desired shape emerges.

The simulations show surprisingly good agreement with the experiment although severe simplifications are done to the experimental geometry. The height of the experimental liquid gap of 40 $\mu$m is too large that the bubble can be considered two-dimensional [18,27] and too small to be a purely axisymmetric one which we assume in the simulations. Yet, our results suggest that the confinement is basically slowing down the dynamics in the projected plane and the bubble shape is in agreement within the spatial and temporal resolution of the experiment. The slowdown of the bubble oscillation in the experiments is approximately 1.7 for all simulations conducted. We suggest that because less liquid is available the fluid acceleration is reduced, which has also been found for a bubble expanding and collapsing within a droplet [30]. Although it is very well established that a single rigid boundary increases the collapse time [13,31], an assessment of the importance of two boundaries

demands a fully three-dimensional simulation.

The flow fields of nonspherical bubbles have interesting properties. For example the torodial bubble possesses a stagnation point at its center. An object placed there would primarily experience a pressure field which may be of interest in the study of pressure-only effects on biological cells.

Chahine and Genoux [32] have developed a Rayleigh-Plesset type model for the oscillation of a toroidal bubble. We have checked their ordinary differential equation against the boundary element method and obtained very good agreement for the overall dynamics and sufficiently large aspect ratios. Interestingly, our simulations reveal the formation of an annular jet during the collapse caused by the inward moving bubble ring. This feature of toroidal bubbles may have not been reported before. Yet, it should be mentioned that toroidal bubbles have been produced with a static hologram and pulsed-laser-illumination before [33].

Except for this jetting the toroidal shape is stable during expansion and collapse; in contrast to the elliptic bubble which demonstrates shape instability during the collapse leading to a rotation of its major axis by 90°. These dynamics are nicely verified in the simulations. We are only aware of one report demonstrating this rotation of the axis for ellipsoidal bubbles [14]. There the ellipsoidal shape is created due to imperfection of the laser focus from the femtosecond optical breakdown process. It is reported that the bubble starting as an ellipsoid obtains an almost spherical shape during maximum expansion, i.e., an aspect ratio of approx. 1.0, and collapses with a 90° rotated major axis. It was argued by Vogel *et al.* [13] that higher curved parts of the bubble shorten the collapse time *locally.* Therefore, more curved parts of the bubble, i.e., closer to the major axis, shrink faster leading to its rotation. This phenomenon is not based on surface tension but inertia only.

The V-shaped bubble accelerates a directed flow from the right to left during in the last stage of collapse, see Figs. 6 and 7; thus a unidirectional jet is obtained from a single bubble, in total absence of boundaries or imposed pressure gradients. This property may be of interest in cavitation assisted microfluidics for the transport of small objects. Also fast and localized jets may be suited to probe elastic properties of microscopic object, e.g., nanotubes and nanowires [34], lipid vesicles, or biological cells.

## VII. CONCLUSIONS

In summary, we have demonstrated the creation and dynamics of nonspherical bubbles in a liquid gap using a pulsed-laser source in combination with a digital hologram. To our knowledge this is the first time that the bubble shape has been altered on-demand. The flows from these bubbles extend the range of flow fields from the well known spherical/hemispherical bubbles in various geometries. They allow to achieve specific tasks, for example unidirectional jetting from the V-shaped bubble and flow with a fixed stagnation point at the center of a toroidal bubble leading to a compressive only flow. On the long term we envision a digitally controlled microfluidic platform actuated with a pulsed laser which allows creating arbitrary flow patterns, manipulate microscopic objects, and measure their elastic properties.

## ACKNOWLEDGMENTS

Funding by the Ministry of Education Singapore (Grant No. T208A1238) and the Nanyang Technological University through Grant No. RG39/07 is greatly acknowledged.

[1] K. R. Rau, P. A. Quinto-Su, A. N. Hellman, and V. Venugopalan, Biophys. J. **91**, 317 (2006).
[2] R. Dijkink, S. Le Gac, E. Nijhuis, A. van den Berg, I. Vermes, A. Poot, and C. D. Ohl, Phys. Med. Biol. **53**, 375 (2008).
[3] P. A. Quinto-Su, H. H. Lai, H. H. Yoon, C. E. Sims, N. L. Allbritton, and V. Venugopalan, Lab Chip **8**, 408 (2008).
[4] H.-H. Lai, P. A. Quinto-Su, C. E. Sims, M. Bachman, G. P. Li, V. Venugopalan, and N. L. Allbritton, J. R. Soc., Interface **5**, S113 (2008).
[5] S. Le Gac, E. Zwaan, A. van den Berg, and C. D. Ohl, Lab Chip **7**, 1666 (2007).
[6] T. H. Wu, L. Gao, Y. Chen, K. Wei, and P.-Yu. Chiou, Appl. Phys. Lett. **93**, 144102 (2008).
[7] A. N. Hellman, K. R. Rau, H. H. Yoon, S. Bae, J. F. Palmer, K. S. Phillips, N. L. Allbritton, and V. Venugopalan, Anal. Chem. **79**, 4484 (2007).
[8] R. Dijkink and C. D. Ohl, Lab Chip **8**, 1676 (2008).
[9] L. V. Zhigilei and B. J. Garrison, J. Appl. Phys. **88**, 1281 (2000).
[10] A. Vogel, J. Noack, K. Nahen, D. Theisen, S. Busch, U. Parlitz, D. X. Hammer, G. D. Noojin, B. A. Rockwell, and R. Birngruber, Appl. Phys. B: Lasers Opt. **68**, 271 (1999).
[11] A. Vogel, Phys. Med. Biol. **42**, 895 (1997).
[12] C. DeMichelis, IEEE J. Quantum Electron. **5**, 188 (1969).
[13] A. Vogel, W. Lauterborn, and R. Timm, J. Fluid Mech. **206**, 299 (1989).
[14] T. Kurz, D. Kröninger, R. Geisler, and W. Lauterborn, Phys. Rev. E **74**, 066307 (2006).
[15] P. A. Quinto-Su, V. Venugopalan, and C. D. Ohl, Opt. Express **16**, 18964 (2008).
[16] Q. X. Wang, K. S. Yeo, B. C. Khoo, and K. Y. Lam, Theor. Comput. Fluid Dyn. **8**, 73 (1996).
[17] S. Rungsiyaphornrat, E. Klaseboer, B. C. Khoo, and K. S. Yeo, Comput. Fluids **32**, 1049 (2003).
[18] E. Zwaan, S. Le Gac, K. Tsuji, and C. D. Ohl, Phys. Rev. Lett. **98**, 254501 (2007).
[19] W. Hentschel and W. Lauterborn, in Proceedings of the First International Conference on Cavitation and Inhomogeneities in Underwater Acoustics, edited by W. Lauterborn (Springer, Berlin, 1980), p. 47.
[20] B. B. Taib, Ph.D. thesis, University of Wollongong, 1985.
[21] G. L. Chahine, in Proceedings IUTAM Symposium, edited by J. R. Blake, J. M. Boulton-Stone, N.H. Thomas (Kluwer Academic Publishers, Birmingham, UK, 1994), p. 195

[22] J. R. Blake, B. B. Taib, and G. Doherty, J. Fluid Mech. **170**, 479 (1986).
[23] E. Klaseboer, S. W. Fong, C. K. Turangan, B. C. Khoo, A. J. Szeri, M. L. Calvisi, G. N. Sankin, and P. Zhong, J. Fluid Mech. **593**, 33-56 (2007).
[24] H. Cole, *Underwater Explosions* (Princeton University Press, Princeton, NJ, 1948).
[25] T. B. Benjamin and A. T. Ellis, Philos. Trans. R. Soc. London, Ser. A **260**, 221 (1966).
[26] N. Bremond, M. Arora, C. D. Ohl, and D. Lohse, Phys. Rev. Lett. **96**, 224501 (2006).
[27] P. A. Quinto-Su and C. D. Ohl, J. Fluid Mech. **633**, 425 (2009).
[28] M. Frenz, G. Paltauf, and H. Schmidt-Kloiber, Phys. Rev. Lett. **76**, 3546 (1996).
[29] G. Paltauf and P. E. Dyer, Chem. Rev. **103**, 487 (2003).
[30] D. Obreschkow, P. Kobel, N. Dorsaz, A. de Bosset, C. Nicollier, and M. Farhat, Phys. Rev. Lett. **97**, 094502 (2006).
[31] J. R. Krieger and G. L. Chahine, J. Acoust. Soc. Am. **118**, 2961 (2005).
[32] G. L. Chahine and P. F. Genoux, J. Fluids Eng. Trans. ASME **105**, 400 (1983).
[33] Paul Prentice, Dundee University (private communication).
[34] P. A. Quinto-Su, X. H. Huang, R. Gonzalez-Avila, T. Wu, and C. D. Ohl, Phys. Rev. Lett. **104**, 014501 (2010).